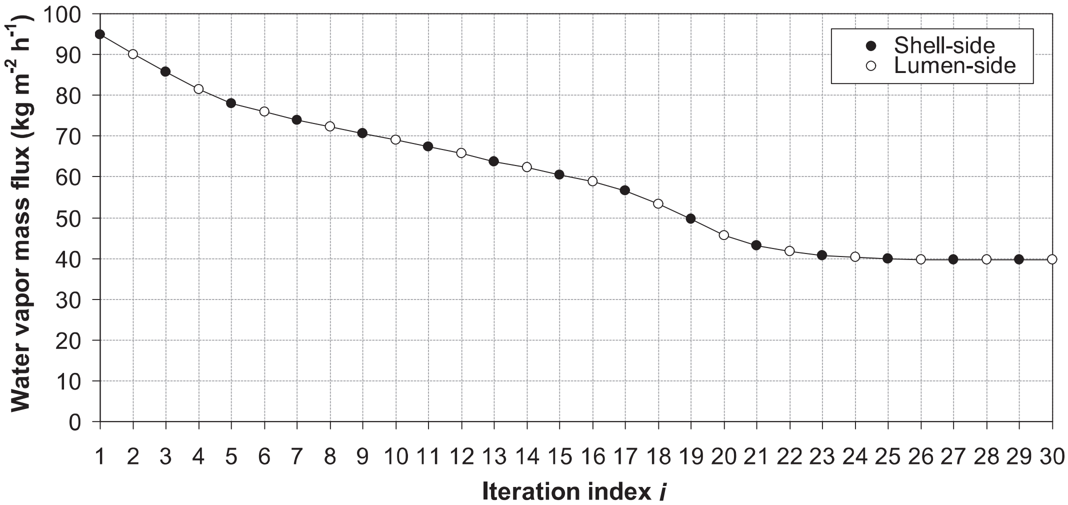

Fig. 5. An example of convergence achieved in the average water vapor mass flux for a simulation case conducted using the rectangular configuration. Solid circles (odd iteration index): shell-side compartment; hollow circles (even iteration index): lumen-side compartment.

2.8. Applicability of the model

The model does not rely on any "adjustable" coefficients and therefore does not require any *ad hoc* calibration. As a result, it can be readily applied to membrane modules of arbitrary design and a wide range of operating conditions. If, however, the feed and permeate streams are arranged such that they occupy the lumen and shell sides in the opposite configuration to that considered here, an appropriate interchange of the "p" and "f" subscripts must be applied.

3. Results

3.1. Rectangular geometry

Consider first the rectangular test section investigated by Song et al. [14] and schematically shown in Fig. 2. In these tests, the feed was tap water at an inlet concentration of 0.58 mol m^{-3} (~0.034 g/L = 34 ppm), see Table 3. In all cases, the temperature at the inlet on the permeate and feed compartments were $T_{p,in}$ = 293.15 K and $T_{f,in}$ = 363.15 K. The permeate inlet flow rate was $Q_{p,in}$ = 1.67·10^{-4} m^3 s^{-1} while the feed inlet flow rate, $Q_{f,in}$, was made to vary between 3.66·10^{-4} and 8.66·10^{-4} m^3 s^{-1}. The lower bound of this range, $Q_{f,in}$ = 3.66·10^{-4} m^3 s^{-1},

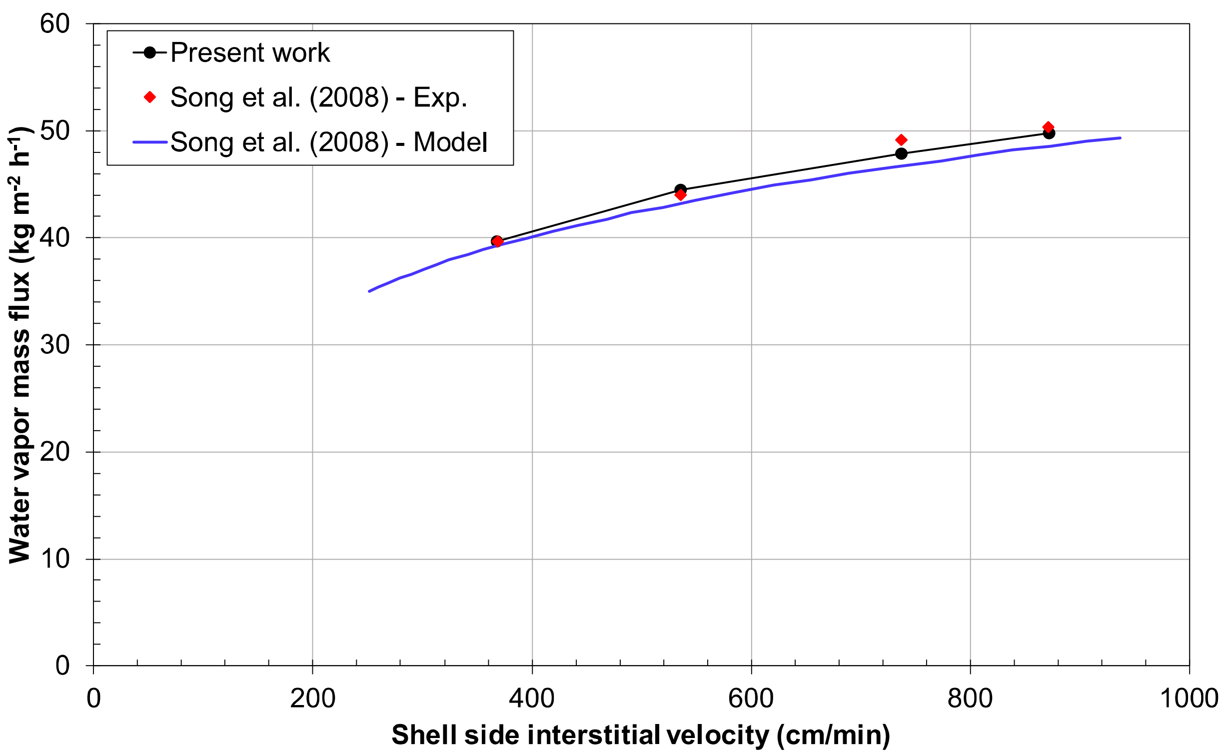

Fig. 6. Average water vapor mass flux as a function of the shell side interstitial velocity, u_{max}, for the rectangular cross flow geometry. Operative conditions: $Q_{p,in}$ = 1.67·10^{-4} m^3 s^{-1}, $T_{p,in}$ = 293.15 K, $T_{f,in}$ = 363.15 K, $C_{f,in}$ = 34 ppm. Results obtained with the present model (thin black line with solid black circles) are compared with both the experiments (red diamonds) and simulations (solid blue line) from Song et al. [14]. (For interpretation of the references to colour in this figure legend, the reader is referred to the web version of this article.)

corresponds to a mean velocity in the narrowest section of the fiber array, u_{max}, of 368 cm/min (0.0613 m s^{-1}) and to a maximum Reynolds number $Re_{f,max} \approx 119$. The upper bound, $Q_{f,in} = 8.66 \cdot 10^{-4}$ m^3 s^{-1}, corresponds to $u_{max} = 872$ cm/min (0.145 m s^{-1}) and $Re_{f,max} \approx 281$. For validation purposes, the same conditions were reproduced in the present numerical simulations. Note that Song et al. [14], in their work, call the quantity u_{max} "interstitial velocity".

Fig. 6 reports the water vapor mass flux as a function of this shell-side interstitial velocity. Red diamond symbols represent the experimental results of Song et al. [14]; the solid blue line represents the predictions obtained by the same authors, and reported in Reference [14], using an in-house DCMD cross-flow hollow-fiber computational model [19]; the thin black line with solid black circles corresponds to the results obtained by the present CFD porous media model.

The present results match the experimental measurements to within ±3%, better than the simulations in [14]. It should be noted that the simulation model in [14] is two-dimensional and therefore does not account for lateral non-uniformities (e.g. for the effects of side walls), whereas the present porous-media model is fully three-dimensional. Moreover, the present model and that in [14] use different formulations for the lumen-side Nusselt number Nu_p. What is more important, CFD predictions correctly capture the data trend, which indicates an increase of the water vapor mass flux with the feed flow rate, its average value $\rho J_{vap,avg}$ rising from ~40 to ~50 kg m^{-2} h^{-1} when the interstitial velocity increases from 368 to 876 cm/min. In the range investigated, the experimental recovery ratio (freshwater yield/feed water flow rate) decreases with $Q_{f,in}$ from 3.85% to 2.03% (of course, this quantity is not particularly significant in a laboratory-scale unit).

The following **Figs. 7 and 8** show selected computational results obtained for this configuration using the present CFD porous media model at an interstitial shell-side velocity of 368 cm/min ($Q_{f,in} = 3.66 \cdot 10^{-4}$ m^3 s^{-1}). The permeate inlet flow rate is $Q_{p,in} = 1.67 \cdot 10^{-4}$ m^3 s^{-1}.

Fig. 7(a) reports a map of the permeate temperature T_p on a *yz* plane through the cold permeate fluid (lumen side compartment). The temperature T_p increases along *z* (direction of the fibers) due to sensible and latent heat inflow from the feed, while it decreases along *y* (direction of the feed) as a consequence of the cooling of the feed fluid along its path.

Fig. 7(b) reports a corresponding map of the feed temperature T_f on the same *yz* plane for the hot feed fluid (shell side compartment). The temperature T_f decreases along the direction of the feed (*y* axis) as a consequence of sensible and latent heat outflow towards the permeate and increases slightly along the direction of the permeate fluid (*z* axis) as a consequence of the heating of the permeate along its path.

As typically occurs in cross-flow heat exchangers, minimum and maximum temperatures are attained at opposite corners of the section considered. Negligible temperature variations, associated only with the presence of side walls, occur along the third direction *x* (not shown).

Fig. 8(a) reports a map of the water vapor mass source term S_W, Eq. (8) with a minus sign, on the same *yz* plane through the hot, shell side fluid considered in Fig. 7(b). Note that S_W is represented in the figure by its absolute value but it acts as a negative (sink) term in the continuity equation of the feed water fluid, Eq. (3). The complex distribution of this term, which is approximately proportional to the temperature difference between feed and permeate, is a consequence of the distributions of feed and permeate temperatures shown in Fig. 7 above.

Fig. 8(b) reports a map of the salt concentration C_f on the same *yz* plane through the shell side (feed-retentate) compartment. The concentration exhibits an opposite behavior with respect to the temperature: it increases along the vertical direction (*y* axis) of the feed fluid, as a consequence of the reduction of the feed flow rate along this direction, and decreases slightly along *z* (direction of the permeate in the lumen side). This effect results from the permeate temperature increasing along *z*, which reduces the transmembrane temperature difference, and thus the water vapor flux, near the permeate outlet end compared to the permeate inlet end of the module. This, in turn, leads to a higher vertical velocity of the feed fluid and a correspondingly lower salt concentration near the permeate outlet end compared to the permeate inlet end. Also the salt concentration exhibits maxima and minima at opposite corners of the section shown. Of course, the salt concentration C_p is nil in the permeate compartment.

As shown in Fig. 7(a, b), the feed-to-permeate temperature difference, which is the driving force of the MD process, varies broadly across the module, ranging from ~6 °C to ~36 °C at the flow rates considered. As a consequence, the water vapor mass source term, Fig. 8(a), exhibits a similar variation, from ~5 to ~35 kg/(m^3 s). Although concepts such as recovery and effectiveness are not particularly significant for the laboratory-scale test module considered here, it is worth noting that both the temperature difference and the water vapor mass source term could be made more uniform by increasing the permeate inlet flow rate. This would entail only a modest increase in permeate pumping power, which remains a small fraction of the thermal energy input.

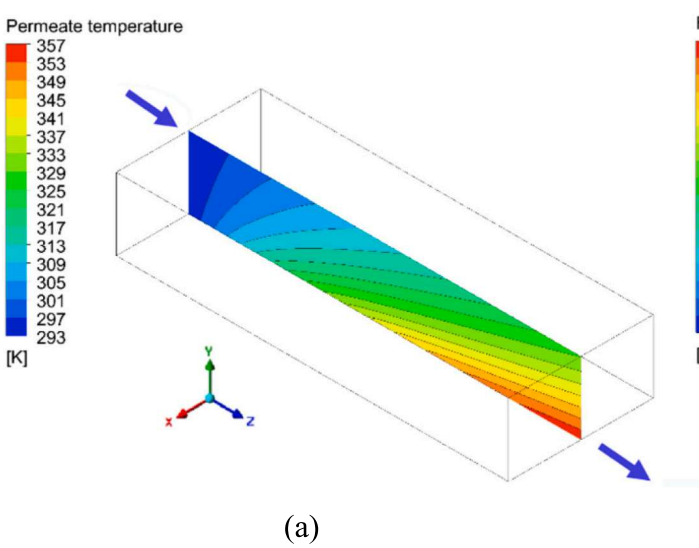

Fig. 7. Contour plots of the temperature (in K) on a *yz* plane for the rectangular cross flow geometry at an interstitial shell-side velocity of 368 cm/min: (a) cold fluid (permeate) and (b) hot fluid (feed). Operative conditions: $Q_{p,in} = 1.67 \cdot 10^{-4}$ m^3 s^{-1}, $Q_{f,in} = 3.66 \cdot 10^{-4}$ m^3 s^{-1}, $T_{p,in} = 293.15$ K, $T_{f,in} = 363.15$ K, $C_{f,in} = 0.58$ mol/m^3. Blue (lumen-side, cold permeate) and red (shell-side, hot feed) arrows indicate the flow direction. (For interpretation of the references to colour in this figure legend, the reader is referred to the web version of this article.)

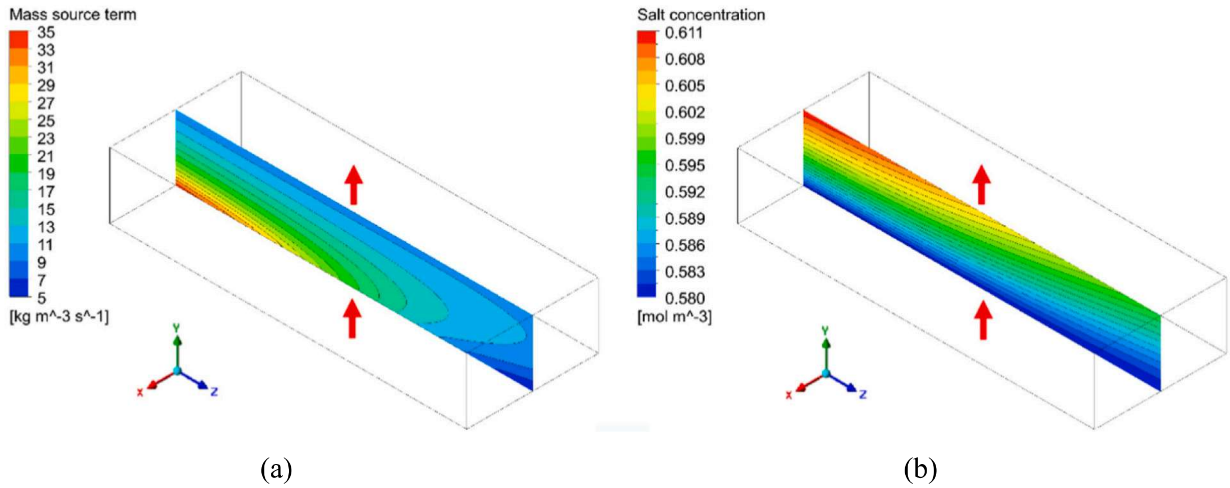

Fig. 8. Contour plots on a *yz* plane through the shell side (feed/retentate) compartment for the rectangular cross flow geometry at an interstitial shell-side velocity of 368 cm/min: (a) water vapor mass source term S_W (in kg m^{-3} s^{-1}) and (b) salt concentration C_f (in mol m^{-3}). Operative conditions: $Q_{p,in} = 1.67 \cdot 10^{-4}$ m^3 s^{-1}, $Q_{f,in} = 3.66 \cdot 10^{-4}$ m^3 s^{-1}, $T_{p,in} = 293.15$ K, $T_{f,in} = 363.15$ K, $C_{f,in} = 0.58$ mol/m^3). Red arrows indicate the flow direction. (For interpretation of the references to colour in this figure legend, the reader is referred to the web version of this article.)

Correspondingly, the currently low recovery ratio, which ranges between ~2% and ~4%, could be significantly improved.

3.2. Cylindrical geometry

Consider now the cylindrical test section denoted as "Large module III – Dead End mode" investigated by Singh et al. [25] and schematically shown in Fig. 3. In these tests, the feed was brackish water with an inlet salt concentration of 171.8 mol m^{-3} (10 g/L = 10,000 ppm), see Table 3. In all cases, the permeate inlet flow rate was $Q_{p,in} = 4.17 \cdot 10^{-5}$ m^3 s^{-1} while the feed inlet flow rate was $Q_{f,in} = 3.00 \cdot 10^{-4}$ m^3 s^{-1}. In the central feeder tube (diameter 2.54×10^{-2} m) the mean velocity was ~0.59 m s^{-1}, corresponding to a Reynolds number of ~38,000. As mentioned in Section 2.3.4, this made it necessary to use a turbulence model for the simulation to converge to a steady-state solution. From the central feeder tube, the feed water flows radially outwards through cylindrical surfaces of length 0.457 m and increasing radius, from 1.27×10^{-2} m to 2.47×10^{-2} m (see Fig. 3). Therefore, the corresponding mean radial (cross flow) velocity, averaged over the entire cylindrical surface (neglecting the fibers), decreases from ~8×10^{-3} to ~4×10^{-3} m s^{-1}. The mean radial velocity in the restricted sections between fibers varies from ~1.79×10^{-2} to ~8.96×10^{-3} m s^{-1} and the corresponding Reynolds number $Re_{f,max}$ from ~28 to ~14, so that the flow in the shell side of the fiber bundle is certainly laminar. The temperature at the inlet on the permeate compartment was $T_{p,in} = 297.15$ K while the feed inlet temperature was made to vary between $T_{f,in} = 348.35$ K and $T_{f,in} = 357.65$ K. For validation purposes, the same conditions were reproduced in the present numerical simulations.

Fig. 9 reports the water vapor mass flux as a function of the shell-side (feed) inlet temperature. Red diamond symbols represent the experimental results of Singh et al. [25]; the solid blue line represents the predictions obtained by the same authors using their own two-dimensional (*r*-*z*) model, implemented in MATLAB; the thin black line with solid black circles corresponds to the results provided by the present 3-D CFD porous media model.

The present results slightly overpredict the experimental

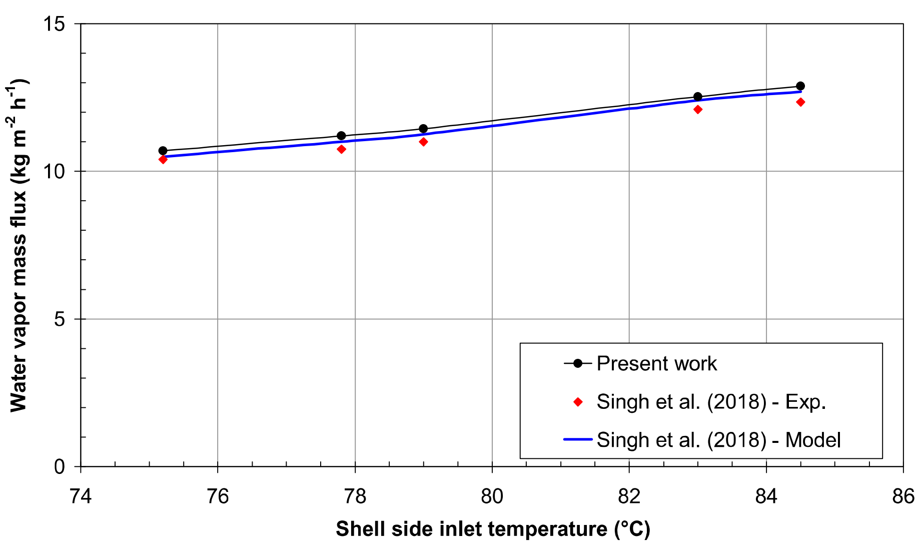

Fig. 9. Average water vapor mass flux as a function of the shell side inlet temperature, $T_{f,in}$, for the cylindrical cross flow geometry. Operative conditions: $Q_{p,in} = 4.167 \cdot 10^{-5}$ m^3 s^{-1} (2.5 L/min), $Q_{f,in} = 3.00 \cdot 10^{-4}$ m^3 s^{-1} (18 L/min), $T_{p,in} = 297.15$ K, $C_{f,in} = 10{,}000$ ppm. Results obtained with the present model (thin black line with solid black circles) are compared with both the experiments (red diamonds) and the simulations (solid blue line) from Singh et al. [25]. (For interpretation of the references to colour in this figure legend, the reader is referred to the web version of this article.)

measurements by up to ~5%, a little more than the simulations in [25]. It is important to observe that the present CFD predictions correctly capture the data trend, which shows an increase of the water vapor mass flux with the feed inlet temperature, its average value $\rho J_{vap,avg}$ rising from ~10.5 kg m^{-2} h^{-1} for $T_{f,in} \approx 75$ °C to ~12.5 kg m^{-2} h^{-1} for $T_{f,in} \approx 85$ °C. For this module, the experimental recovery ratio increases with $T_{f,in}$ from 1.10% to 1.33% (as remarked above, this quantity is not particularly significant in a laboratory-scale unit).

The following Figs. 10 through 12 show selected computational results by the present CFD porous media model for the cylindrical configuration at the following operating conditions: $Q_{p,in} = 4.167 \cdot 10^{-5}$ m^3 s^{-1}, $Q_{f,in} = 3.00 \cdot 10^{-4}$ m^3 s^{-1}, $T_{p,in} = 297.15$ K, $T_{f,in} = 352.15$ K (79 °C).

Fig. 10 shows the temperature distributions on longitudinal (zx) sections of the lumen side (permeate) compartment (a) and of the shell side (feed) compartment (b). Since lumen-side quantities are only defined in the bundle region but not in the central feeder tube, map (a) does not represent the temperature in this latter region. Two different scales are used for the two temperatures; blue and red arrows indicate the permeate and feed inlet and outlet flow, respectively. Note that the fluids flow in counter-current mode, with a feed flow rate almost seven times that of the permeate.

The permeate temperature in Fig. 10(a) varies mainly along the axial direction z, with an initial steep increase near the permeate inlet / feed outlet, where the temperature difference between the two fluids is large (> 40 °C), and a slower variation in the last fraction of the module length, where the two fluids almost attain thermal equilibrium.

An interesting feature of the feed (shell side) temperature distribution, Fig. 10(b), is that the temperature in the central feeder tube decreases along the z axis almost at the same rate as the temperature in the bundle, despite the central feeder tube lacks the cold sink represented by the hollow fibers. The reason for this behavior is the diffusive radial heat flux from the feed fluid flowing in the tube to the surrounding feed fluid flowing in the annular bundle region. Note that radial diffusion is enhanced by turbulence in the tube, explicitly accounted for in the present simulations by the k-ω model used. This phenomenon, which appears to be detrimental for the overall efficiency of the module, might be reduced in the simulations by interposing a physical perforated wall between the central feeder tube and the bundle region (such wall seems to have been present in the experiments, but was not simulated in the model for lack of detailed information).

Fig. 11(a) shows the distribution of the water vapor mass source term S_W, see Eq. (8) written with a minus sign, on the same longitudinal zx section of the bundle region of the shell side (feed) compartment. As discussed above, S_W is not defined (and thus is not represented) in the central feeder tube. Note that S_W actually acts as a sink (negative) term in the continuity equation of the feed fluid, Eq. (3), but is represented in the figure by its absolute value. Consistently with the above remarks on the two fluids attaining thermal equilibrium in the feed inlet / permeate outlet region of the module, here the water vapor flux is very small.

Fig. 11(b) shows the distribution of the salt concentration C_f on the same longitudinal plane of Fig. 11(a), this time including also the central feeder tube. As expected, the salt concentration in the retentate increases along the axis in the annular bundle region because of the selective loss of water towards the hollow fibers and the permeate compartment. In analogy with the corresponding temperature distribution in Fig. 10(b), the salt concentration increases along the module axis also in the central feeder tube despite the lack of water sinks (hollow fibers) herein, as a consequence of radial diffusion of salt from the surrounding annular bundle region into the central feeder tube.

Finally, Fig. 12(a) reports the distribution of the velocity module $|\mathbf{u}|$ on a longitudinal section of the feed (shell side) compartment, including the central feeder tube. Significant velocities, up to 0.7 m s^{-1}, are observed only in the feed inlet region, while velocities decrease rapidly along the z axis as a large fraction of the inlet flow rate exits through the nearest outlet ports. In most of the module volume, velocities are only a few cm s^{-1}.

Fig. 12(b) reports the distribution of the Nusselt number Nu_f, as provided by Eqs. (17), on a longitudinal section of the feed (shell side) compartment, limited, in this case, to the bundle region (Nu_f is not defined in the central feeder tube). Significant values of Nu_f, up to ~35, are attained only near the inlet and outlet regions of the feed path, while very low values characterize the central portion of the bundle. Note, however, that Eqs. (17) from Zukauskas [44] lack a baseline value and predict $Nu_f \to 0$ for $Re_{f,max} \to 0$, which is unphysical.

As for the previous rectangular geometry, considerations of recovery

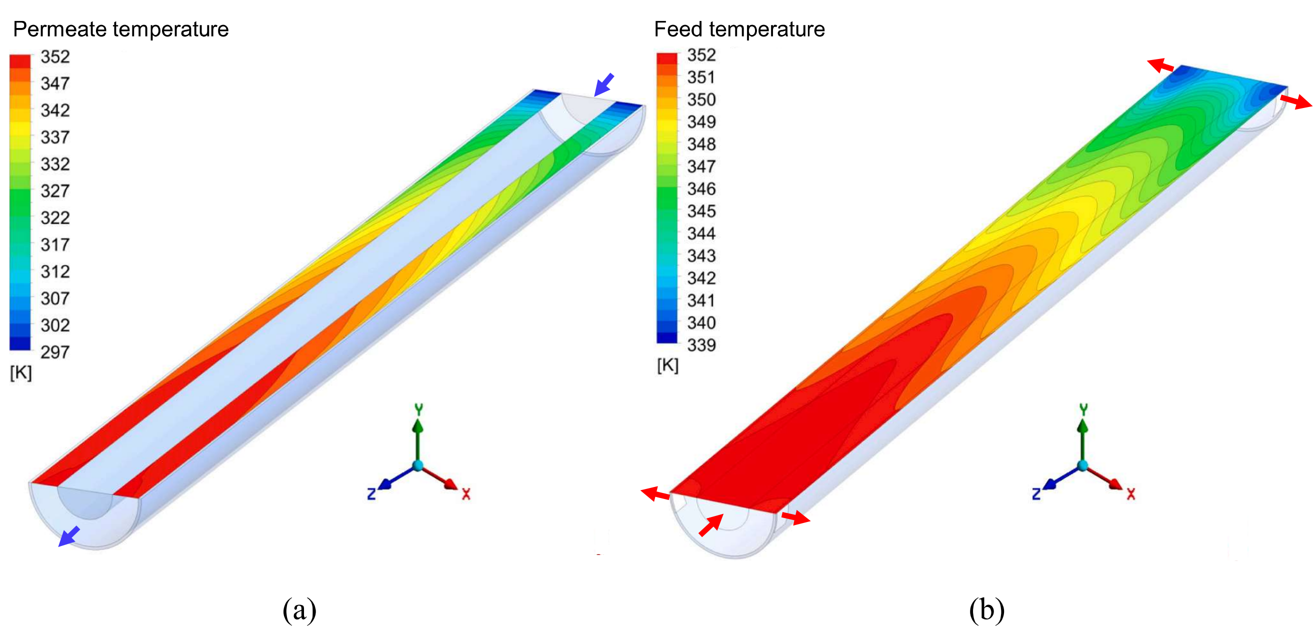

Fig. 10. Contour plots of the temperature (in K) on a zx plane for the cylindrical cross flow geometry at a shell-side inlet temperature $T_{f,in} = 352.15$ K: (a) cold fluid (permeate) and (b) hot fluid (feed) compartment. Operative conditions: $Q_{p,in} = 4.167 \cdot 10^{-5}$ m^3 s^{-1}, $Q_{f,in} = 3.00 \cdot 10^{-4}$ m^3 s^{-1}, $T_{p,in} = 297.15$ K, $C_{f,in} = 171.8$ mol/m^3. Blue (lumen-side, cold fluid) and red (shell-side, hot fluid) arrows indicate the flow direction. (For interpretation of the references to colour in this figure legend, the reader is referred to the web version of this article.)

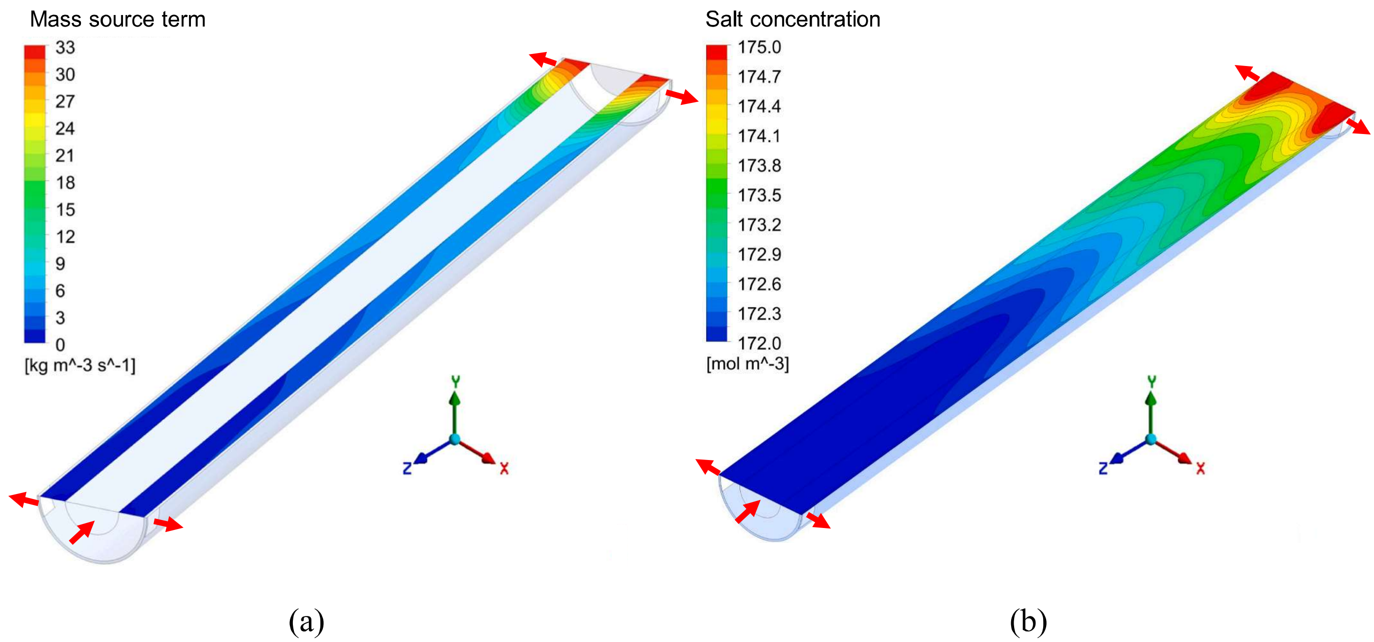

Fig. 11. Contour plots on a *zx* plane through the shell side (feed/retentate) compartment for the cylindrical cross flow geometry at a feed water inlet temperature $T_{f,in} = 352.15$ K: (a) water vapor mass source term S_W (expressed as an absolute value in kg m^{-3} s^{-1}) and (b) salt concentration C_f (in mol m^{-3}). Operative conditions: $Q_{p,in} = 4.167 \cdot 10^{-5}$ m^3 s^{-1}, $Q_{f,in} = 3.00 \cdot 10^{-4}$ m^3 s^{-1}, $T_{p,in} = 297.15$ K, $C_{f,in} = 171.8$ mol/m^3). Red arrows indicate the flow direction. Note that the mass source term is not defined in the central feeder tube region. (For interpretation of the references to colour in this figure legend, the reader is referred to the web version of this article.)

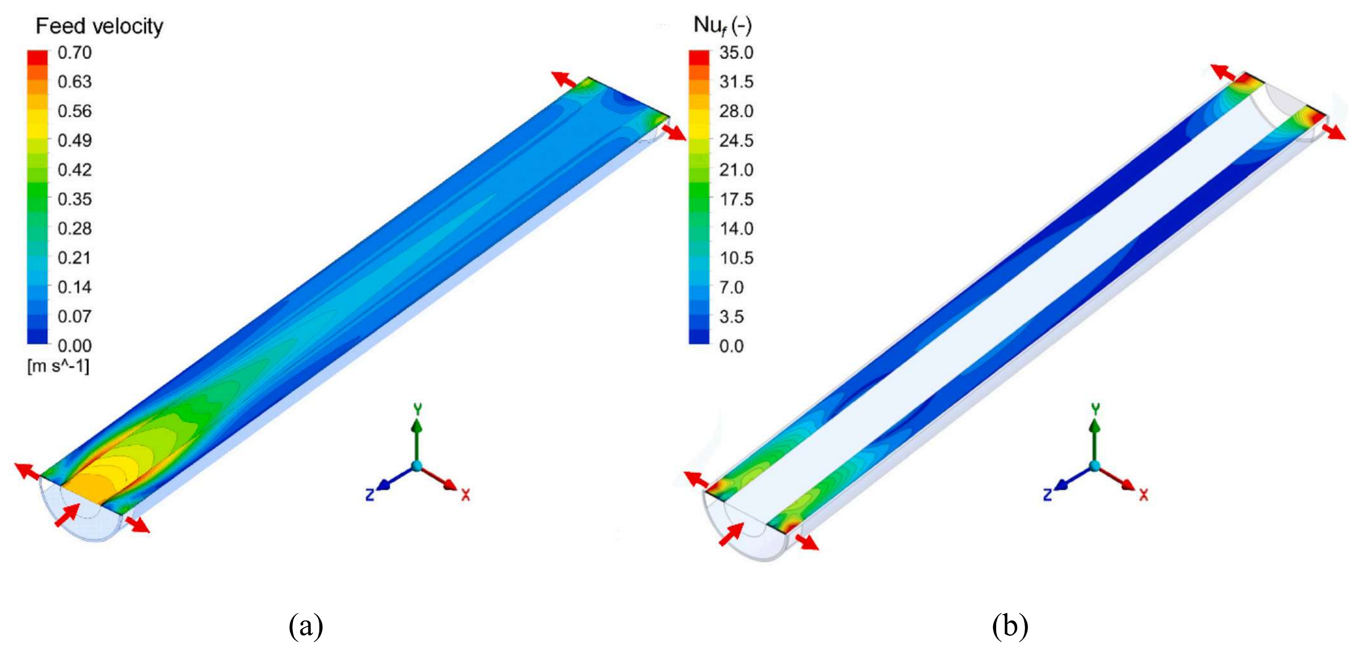

Fig. 12. Contour plots on a *zx* plane through hot fluid (feed/retentate) compartment for the cylindrical cross flow geometry at a shell-side inlet temperature $T_{f,in} = 352.15$ K: (a) velocity module (in m s^{-1}) and (b) Nusselt number (dimensionless). Operative conditions: $Q_{p,in} = 4.167 \cdot 10^{-5}$ m^3 s^{-1}, $Q_{f,in} = 3.00 \cdot 10^{-4}$ m^3 s^{-1}, $T_{p,in} = 297.15$ K, $C_{f,in} = 171.8$ mol/m^3). Red arrows indicate fluid flow direction. (For interpretation of the references to colour in this figure legend, the reader is referred to the web version of this article.)

and effectiveness are of limited relevance for the cylindrical module considered here, which (although larger than the previous one) remains primarily a laboratory-scale test section. Nevertheless, the results indicate potential opportunities for improving both the operating conditions and module design.

Preliminarily, as Fig. 10(a, b) shows, at the flow rates considered the feed-to-permeate temperature difference varies widely across the module, ranging from ~42 °C near the permeate inlet to nearly zero near the permeate outlet. Consequently, the water vapor mass source term, Fig. 11(a), varies similarly, from ~33 kg/(m^3 s) down to ~0, meaning that different regions of the module contribute very unevenly to freshwater production. The temperature difference could be increased and made more uniform by raising the permeate inlet flow rate, which is currently ~8 times lower than the feed flow rate. This adjustment would greatly enhance the water vapor flux, thereby increasing freshwater yield and the recovery ratio, which is currently very low (~1.1%–1.3%, depending on the feed inlet temperature).

In regard to module design, the computational results indicate that a large fraction of the feed exits the module through the nearest outlets without significantly contributing to mass transfer. This suggest that the current location and hydraulic resistance of the shell-side outlets, along with the design of the perforated central feeder tube, appear to be quite ineffective. Optimizing these elements together could help achieve a more uniform radial feed-retentate flow through the annular fiber bundle. Such optimization could be pursued through a combination of numerical simulations and relatively simple experiments, for example using dye tracers to visualize flow distribution in alternative configurations.

Finally, it should be noted that questions of overall effectiveness or cost cannot be resolved by considering a single module, without heat recovery. These issues can only be addressed by evaluating the whole plant layout, including heat exchangers, water heaters, and other systems components.

4. Conclusions

A three-dimensional, CFD-based, porous media model was developed to predict the flow, temperature and salt concentration fields and the overall performance of hollow fiber Direct Contact Membrane Distillation modules. The model was validated against two different sets of experimental results, for city and brackish water, presented in the literature for laboratory-scale modules.

In both cases, lumen side friction coefficient and Nusselt number were derived from the assumption of Poiseuille flow. For the shell side Darcy permeability, the values computed in previous fully developed unit-cell CFD simulations were adopted. The shell-side Nusselt number was obtained from classic correlations of Zukauskas [44] for cross flow past tube banks.

The first test case regarded a rectangular configuration [14]. Here, the cold permeate flowed in the lumen of hollow fibers arranged in a rectangular staggered pattern with a bundle porosity of 0.791. The hot feed flowed in the shell side orthogonally to the fibers. In the experiments, the authors let the feed flow rate vary so that the interstitial velocity ranged between 0.0613 and 0.146 m s^{-1}. In the simulations, for the membrane permeance and equivalent thermal conductivity, the same values reported by the authors of the experiments were used. The present CFD simulations reproduced well (within a few percent) the experimental values of the water vapor flux (i.e., of the module's yield) and its positive correlation with the feed flow rate.

The second test case regarded a cylindrical configuration [25]. Here, the cold permeate flowed, as in the previous case, in the lumen of hollow fibers, which were now arranged in an approximately concentric-circle pattern within a cylinder casing, with a bundle porosity of 0.76. The hot feed flowed radially in the shell side from an inner cylindrical feeder tube to an outer cylindrical sleeve, again orthogonally (i.e., in cross flow) with respect to the fibers. In these experiments, the authors let the feed inlet temperature vary between ~75 °C and ~ 85 °C. In the simulations, as in the previous case, membrane permeance and equivalent thermal conductivity were those reported by the authors of the experiments. The present CFD simulations reproduced with satisfactory accuracy the experimental values of the water vapor flux and its positive correlation with the feed inlet temperature.

Two notable aspects can be highlighted. (i) Despite the highly complex computational procedure, the model is able to converge thanks to the use of an under-relaxation factor; (ii) the CFD model presented here is capable to satisfactorily predict experimental findings from two different geometric configurations.

As anticipated in the Introduction section, the use of a CFD-based model, albeit in the porous media approximation, proved to be highly effective in revealing aspects of the complex physical phenomena occurring in an MD module, as shown, for example, by the discussion of Figs. 7–8 and Figs. 10–12, and in highlighting weak design spots and suggesting potential improvements.

Thus validated, the model presented here will be employed to perform a sensitivity analysis of the hollow fiber membrane distillation module's performance with respect to key control parameters, including:

- Hollow fiber membrane properties. Among these, those directly affecting a module performance are fiber geometry (diameter and thickness) and membrane permeance and thermal conductivity, which depend in their turn on its composition (polymeric matrix) and microscale morphology (porosity, pore tortuosity, mean value and distribution of pore diameter).
- Design options. For example, these include the choice of a cross flow versus an axial flow configuration and of a rectangular versus a cylindrical layout; the location and geometry of inlets and outlets; the module aspect ratio.
- Operating conditions. The investigation of different inlet flow rates and temperatures of feed and permeate, and different feed water salt concentrations.
- Fiber bundle porosity. For example, unit cell simulations by our research group [31] indicate that, as the porosity decreases from 0.6 to 0.4, the shell side Nusselt number in cross flow increases significantly, thus reducing temperature polarization.
- Fiber bundle lattice. The same study [31] indicates that the shell side Nusselt number in cross flow is much larger for regular fiber arrays (in particular, hexagonal arrays) than for random fiber distributions.
- Feed side configuration. The choice of the *outside-in* configuration, with feed on the shell side and permeate on the lumen side, as in the present test cases, or the *inside-out* one, deserves further attention.

The module-scale model will also serve as a foundation component of a larger-scale, plant-level, modelling platform, capable of capturing the interactions and mutual constraints among coupled system components. For example, the authors are currently exploring the use of Membrane Distillation as a source of ultrapure water for electrolyzers in green hydrogen production. In this configuration, waste heat from the electrolyzer would be used to heat the MD feed water, and optimal operating temperatures must be determined for the integrated system rather than for each component individually. Many other examples of component coupling exist, such as brine volume reduction in Reverse Osmosis, wastewater treatment, and various process chains, all involving MD at some stage. In each case, a reliable MD unit model is essential to accurately predict and optimize system performance.

In regard to model improvements aiming at making it fully predictive, one important step forward will be the derivation of membrane permeance and equivalent thermal conductivity from the membrane composition and microscale morphology, using the best available models of transmembrane heat and mass transfer [47] rather than relying on empirical or best-fit values. However, "microscopic" data are generally not available with sufficient accuracy (for instance, determining the pore tortuosity is notoriously difficult), so some degree of empirical input would likely still be necessary.

A second step forward will be the use of advective heat transfer correlations based on fiber-scale CFD simulations *in lieu* of literature correlations like Zukauskas' which, however authoritative, are rather outdated, physically inconsistent for lack of a baseline Nu value for Re → 0, and little suitable for the fiber arrangements and Reynolds number ranges typical of hollow fiber DCMD.

CRediT authorship contribution statement

N. Cancilla: Writing – original draft, Visualization, Validation, Software, Methodology, Investigation, Formal analysis, Data curation, Conceptualization. **M. Ciofalo:** Writing – review & editing, Validation, Supervision, Software, Methodology, Formal analysis, Data curation, Conceptualization. **A. Tamburini:** Writing – review & editing, Validation, Supervision, Resources, Project administration, Data curation, Conceptualization. **G. Micale:** Writing – review & editing, Supervision, Resources, Project administration, Funding acquisition, Conceptualization.

Declaration of competing interest

The authors declare that they have no known competing financial interests or personal relationships that could have appeared to influence the work reported in this paper.

Acknowledgments

Partially funded by the European Union – Next Generation EU - PNRR M4 – C2 - investment 1.1: *Fondo per il Programma Nazionale di Ricerca e Progetti di Rilevante Interesse Nazionale* (PRIN) - PRIN 2022PNRR cod. P20225HTWF titled "*An ab-initio multi-scale-unit computational procedure for sustainable production of fresh water through circular integration of desalination and forward osmosis*" - CUP B53D23026770001.

References

[1] K. Harby, M. Emad, M. Benghanem, T.Z. Abolibda, K. Almohammadi, A. Aljabri, A. Alsaiari, M. Elgendi, Reverse osmosis hybridization with other desalination techniques: an overview and opportunities, Desalination 581 (2024) 117600, https://doi.org/10.1016/j.desal.2024.117600.

[2] C. Skuse, A. Gallego-Schmid, A. Azapagic, P. Gorgojo, Can emerging membrane-based desalination technologies replace reverse osmosis? Desalination 500 (2021) 114844 https://doi.org/10.1016/j.desal.2020.114844.

[3] A. Cipollina, M.G. Di Sparti, A. Tamburini, G. Micale, Development of a membrane distillation module for solar energy seawater desalination, Chem. Eng. Res. Design 90 (2012) 2101–2121, https://doi.org/10.1016/j.cherd.2012.05.021.

[4] Y.M.C. Manawi, M.A. Khraisheh, A.K.C. Fard, F.A. Benyahia, S. Adham, Effect of operational parameters on distillate flux in direct contact membrane distillation (DCMD): comparison between experimental and model predicted performance, Desalination 336 (2014) 110–120, https://doi.org/10.1016/j.desal.2014.01.003.

[5] L. Eykens, I. Hitsov, K. De Sitter, C. Dotremont, L. Pinoy, I. Nopens, Van der bruggen, Influence of membrane thickness and process conditions on direct contact membrane distillation at different salinities, J. Membr. Sci. 498 (2016) 353–364, https://doi.org/10.1016/j.memsci.2015.07.037.

[6] M.S. El-Bourawi, Z. Ding, R. Ma, M. Khayet, A framework for better understanding membrane distillation separation process, J. Membr. Sci. 285 (2006) 4–29, https://doi.org/10.1016/j.memsci.2006.08.002.

[7] G. Rácz, S. Kerker, Z. Kovács, G. Vatai, M. Ebrahimi, P. Czermak, Theoretical and experimental approaches of liquid entry pressure determination in membrane distillation processes, Period. Polytech. Chem. Eng. 58 (2014) 81–91, https://doi.org/10.3311/PPch.2179.

[8] M. Khayet, T. Matsuura, Membrane Distillation - Principles and Applications, Elsevier, 2011. ISBN 978–0–444-53126-1. doi:https://doi.org/10.1016/C2009-0-17487-1.

[9] B.B. Ashoor, S. Mansour, A. Giwa, V. Dufour, S.W. Hasan, Principles and applications of direct contact membrane distillation (DCMD): a comprehensive review, Desalination 398 (2016) 222–246, https://doi.org/10.1016/j.desal.2016.07.043.

[10] M. Khayet, Membranes and theoretical modeling of membrane distillation: a review, Adv. Colloid Interf. Sci. 164 (2011) 56–88, https://doi.org/10.1016/j.cis.2010.09.005.

[11] H. Lee, F. He, L. Song, J. Gilron, K.K. Sirkar, Desalination with a cascade of crossflow hollow fiber membrane distillation devices integrated with a heat exchanger, AICHE J. 57 (2011) 1780–1795, https://doi.org/10.1002/aic.12409.

[12] J.L. Gilron, L. Song, K.K. Sirkar, Design for cascade of cross-flow direct contact membrane distillation, Ind. Eng. Chem. Res. 46 (2007) 2324–2334, https://doi.org/10.1021/ie060999k.

[13] R. Ullah, M. Khraisheh, R.J. Esteves, J.T. McLeskey Jr., M. AlGhouti, M. Gad-el-Hak, H.V. Tafreshi, Energy efficiency of direct contact membrane distillation, Desalination 433 (2018) 56–67, https://doi.org/10.1016/j.desal.2018.01.025.

[14] L. Song, Z. Ma, X. Liao, P.B. Kosaraju, J.R. Irish, K.K. Sirkar, Pilot plant studies of novel membranes and devices for direct contact membrane distillation-based desalination, J. Membr. Sci. 323 (2008) 257–270, https://doi.org/10.1016/j.memsci.2008.05.079.

[15] H. Kariman, H.A. Mohammed, M. Zargar, M. Khiadani, Performance comparison of flat sheet and hollow fibre air gap membrane distillation: a mathematical and simulation modelling approach, J. Membr. Sci. 721 (2025) 123836, https://doi.org/10.1016/j.memsci.2025.123836.

[16] N. Cancilla, L. Gurreri, M. La Rosa, M. Ciofalo, A. Cipollina, A. Tamburini, G. Micale, Influence of bundle porosity on shell-side hydrodynamics and mass transfer in regular fiber arrays: a computational study, Int. J. Heat Mass Transf. 203 (2023) 123841, https://doi.org/10.1016/j.ijheatmasstransfer.2022.123841.

[17] C.F. Wan, T. Yang, G.G. Lipscomb, D.J. Stookey, T.-S. Chung, Design and fabrication of hollow fiber membrane modules, in: Hollow Fiber Membranes, Elsevier, 2021, pp. 225–252, https://doi.org/10.1016/B978-0-12-821876-1.00007-X.

[18] B. Li, K.K. Sirkar, Novel membrane and device for direct contact membrane distillation-based desalination process, Ind. Eng. Chem. Res. 43 (2004) 5300–5309, https://doi.org/10.1021/ie030871s.

[19] L. Song, B. Li, K.K. Sirkar, J.L. Gilron, Direct contact membrane distillation-based desalination: novel membranes, devices, larger-scale studies, and a model, Ind. Eng. Chem. Res. 46 (2007) 2307–2323, https://doi.org/10.1021/ie0609968.

[20] B. Li, K.K. Sirkar, Novel membrane and device for vacuum membrane distillation-based desalination process, J. Membr. Sci. 257 (2005) 60–75, https://doi.org/10.1016/j.memsci.2004.08.040.

[21] D. Singh, K.K. Sirkar, High temperature direct contact membrane distillation based desalination using PTFE hollow fibers, Chem. Eng. Sci. 116 (2014) 824–833, https://doi.org/10.1016/j.ces.2014.05.042.

[22] L. Li, L. Song, K.K. Sirkar, Desalination performances of large hollow Fiber-based DCMD devices, Ind. Eng. Chem. Res. 56 (2017) 1594–1603, https://doi.org/10.1021/acs.iecr.6b04037.

[23] D. Singh, P. Prakash, K.K. Sirkar, De-oiled produced water treatment using direct-contact membrane distillation, Ind. Eng. Chem. Res. 52 (2013) 13439–13448, https://doi.org/10.1021/ie4015809.

[24] C. Webb, L.N.S.P. Nagghappan, G. Smart, J. Hoblitzell, R. Franks, Desalination of oilfield-produced water at the San Ardo water reclamation facility, SPE Western Regional Meeting, San Jose, California, 2009, p. 121520, https://doi.org/10.2118/121520-MS.

[25] D. Singh, L. Li, G. Obusckovic, J. Chau, K.K. Sirkar, Novel cylindrical cross-flow hollow fiber membrane module for direct contact membrane distillation-based desalination, J. Membr. Sci. 545 (2018) 312–322, https://doi.org/10.1016/j.memsci.2017.09.007.

[26] F. He, K.K. Sirkar, J. Gilron, Studies on scaling of membranes in desalination by direct contact membrane distillation: CaCO3 and mixed CaCO3/CaSO4 systems, Chem. Eng. Sci. 64 (2009) 1844–1859, https://doi.org/10.1016/j.ces.2008.12.036.

[27] F. He, K.K. Sirkar, J. Gilron, Effects of antiscalants to mitigate membrane scaling by direct contact membrane distillation, J. Membr. Sci. 345 (2009) 53–58, https://doi.org/10.1016/j.memsci.2009.08.021.

[28] A.K. Sharma, A. Juelfs, C. Colling, S. Sharma, S.P. Conover, A.A. Puranik, J. Chau, L. Rodrigues, K.K. Sirkar, Porous hydrophobic– hydrophilic composite hollow fiber and flat membranes prepared by plasma polymerization for direct contact membrane distillation, Membranes (Basel) 11 (2021) 120, https://doi.org/10.3390/membranes11020120.

[29] F. Liu, W. Qing, G. Zhu, Q. Ma, J. Chau, K.K. Sirkar, W. Zhang, A two hollow-fiber-set membrane module for air gap membrane distillation with high thermal efficiency, Desalination 604 (2025) 118683, https://doi.org/10.1016/j.desal.2025.118683.

[30] K.M. Lisboa, J.R.B. de Souza, C.P. Naveira-Cotta, R.M. Cotta, Heat and mass transfer in hollow-fiber modules for direct contact membrane distillation: integral transforms solution and parametric analysis, Int. Commun. Heat Mass Transf. 109 (2019) 104373, https://doi.org/10.1016/j.icheatmasstransfer.2019.104373.

[31] N. Cancilla, A. Bounou, M. Ciofalo, A. Tamburini, G. Micale, CFD prediction of flow and heat transfer in hollow fiber bundles for membrane distillation: a comparison of regular and random arrangements, Int. J. Heat Mass Transf. 254 (2026) 127672, https://doi.org/10.1016/j.ijheatmasstransfer.2025.127672.

[32] A.S. Kim, Cylindrical cell model for direct contact membrane distillation (DCMD) of densely packed hollow fibers, J. Membr. Sci. 455 (2014) 168–186, https://doi.org/10.1016/j.memsci.2013.12.067.

[33] K. Marques Lisboa, D. Busson de Moraes, C. Palma Naveira-Cotta, R. Machado Cotta, Analysis of the membrane effects on the energy efficiency of water desalination in a direct contact membrane distillation (DCMD) system with heat recovery, Appl. Therm. Eng. 182 (2021) 116063, https://doi.org/10.1016/j.applthermaleng.2020.116063.

[34] N. Cancilla, L. Gurreri, G. Marotta, M. Ciofalo, A. Cipollina, A. Tamburini, G. Micale, A porous media CFD model for the simulation of hemodialysis in hollow fiber membrane modules, J. Membr. Sci. 646 (2022) 120219, https://doi.org/10.1016/j.memsci.2021.120219.

[35] W. Ding, W. Li, S. Sun, X. Zhou, P.A. Hardy, S. Ahmad, D. Gao, Three-dimensional simulation of mass transfer in artificial kidneys, Artif. Organs 39 (2015) E79–E89, https://doi.org/10.1111/aor.12415.

[36] D. Chen, B. Lakghomi, Y. Lawryshyn, Evaluation of using a porous medium approach to simulate flat-sheet membrane bioreactors, Water Sci. Technol. 86 (2022) 746–762, https://doi.org/10.2166/wst.2022.235.

[37] X. Yao, V. Freger, X. He, R. Wang, B. Kong, Three-dimensional CFD modeling for hollow fiber gas separation membrane modules based on a dual porous media model, Chem. Eng. Sci. 302 (2025) 120864, https://doi.org/10.1016/j.ces.2024.120864.

[38] ANSYS, Inc., ANSYS-CFX Reference Guide 2023 R2, 2023.

[39] S.T. Bouguecha, S.E. Aly, M.H. Al-Beirutty, M.M. Hamdi, A. Boubakri, Solar driven DCMD: performance evaluation and thermal energy efficiency, Chem. Eng. Res. Des. 100 (2015) 331–340, https://doi.org/10.1016/j.cherd.2015.05.044.

[40] L. Eykens, I. Hitsov, K. De Sitter, C. Dotremont, L. Pinoy, I. Nopens, B. Van der Bruggen, Influence of membrane thickness and process conditions on direct contact membrane distillation at different salinities, J. Membr. Sci. 498 (2016) 353–364, https://doi.org/10.1016/j.memsci.2015.07.037.

[41] Z. Kuang, R. Long, Z. Liu, W. Liu, Analysis of temperature and concentration polarizations for performance improvement in direct contact membrane distillation, Int. J. Heat Mass Transf. 145 (2019) 118724, https://doi.org/10.1016/j.ijheatmasstransfer.2019.118724.
[42] C. Lai, H. Zhang, An efficient and economic evacuated u-tube solar collector powered air gap membrane distillation hybrid system for seawater desalination, J. Clean. Prod. 394 (2023) 136382, https://doi.org/10.1016/j.jclepro.2023.136382.
[43] T. Bergman, A. Lavine, F. Incropera, D. Dewitt, Fundamentals of Heat and Mass Transfer, 7th ed., John Wiley & Sons, 2011.
[44] A. Žukauskas, Heat transfer from tubes in cross-flow, Adv. Heat Tran. 8 (1972) 93–160, https://doi.org/10.1016/S0065-2717(08)70038-8.
[45] D.C. Wilcox, Reassessment of the scale-determining equation for advanced turbulence models, AIAA J. 26 (1988) 1299–1310, https://doi.org/10.2514/3.10041.
[46] N. Cancilla, L. Gurreri, G. Marotta, M. Ciofalo, A. Cipollina, A. Tamburini, G. Micale, CFD prediction of shell-side flow and mass transfer in regular fiber arrays, Int. J. Heat Mass Transf. 168 (2021) 120855, https://doi.org/10.1016/j.ijheatmasstransfer.2020.120855.
[47] N. Cancilla, A. Cipollina, L. Gurreri, M. Ciofalo, Direct contact membrane distillation: a critical review of transmembrane heat and mass transfer models, Membranes (Basel) 16 (2026) 64, https://doi.org/10.3390/membranes16020064.
[48] A. Giordano, N. Cancilla, M. Ciofalo, D. Donato, G. Marotta, G. Micale, A. Tamburini, Shell-side friction and mass transfer along bundles of undulated fibers, Chem. Eng. Sci. 309 (2025) 121406, https://doi.org/10.1016/j.ces.2025.121406.